Error Correction for Diffraction and Multiple Scattering in Free-Space Microwave Measurement of Materials

Kai Meng Hock

***Abstract*—Metamaterials often have sharp resonances in permittivity or permeability at microwave frequencies. The sizes of the inclusions are of the order of millimeters, and this means that it is more convenient to carry out the measurement in free space. Time gating is often used in the free-space method to remove multiple scattering from the antennas and the surrounding objects. However, this lowers the resolution in the frequency domain, making it difficult to resolve the resonances reliably. Diffraction around the sample could also reduce measurement accuracy. A calibration procedure, based on the 16-term error model, which removes the need for time gating by correcting for both multiple scattering and diffraction, is developed. This procedure is tested on carbonyl iron composite and split-ring resonators, and the results are presented.**

***Index Terms*—Error correction, free-space measurement, metamaterials, microwave, split-ring resonators (SRRs).**

I. Introduction

THIS STUDY is motivated by the need to measure sharp resonances in the permittivity or the permeability of metamaterials. These materials may consist of elements of straight wires, split rings, or even helices and could have a resonance width of 0.1 GHz or less [1]–[4]. The sizes of these elements are typically of the order of millimeters, and their resonances occur at microwave frequencies. A large variety of methods exist for the measurement of microwave properties of materials. For broad-band measurements, two of the commonly used methods are the free-space method [5]–[8] and the coaxial waveguide method [9], [10]. The sizes of the metamaterial elements make it difficult to insert enough of the material into a coaxial airline, which is typically 7 or 14 mm in diameter. While it is possible to make coaxial waveguides of larger diameters, the cylindrical symmetry of the guided plane wave would complicate the interpretation of the scattered waves. The free-space method, therefore, offers more convenience and greater simplicity in these respects.

In the free-space method, a slab of the metamaterial may be placed in between two antennas facing each other, and the transmission and reflection coefficients measured. There are a few disadvantages to this setup. The near-field position of the sample means that the wavefront would not, in general, be planar. The finite size of the sample allows diffraction of the microwave around the edges of the sample in a transmission measurement. There is also multiple scattering between sample and antennas. There have been attempts to produce planar wavefront and reduce diffraction by using spot-focusing antennas [5]. However, the effect of this is difficult to characterize for every setup. The focusing also reduces the number of elements in the metamaterials that are being sampled by the microwave. Multiple scattering can be removed by time gating. However, for a narrow resonance, the time-domain response of the metamaterial may extend beyond the first reflection from the antenna. If this happens, time gating would remove part of the response. This would reduce the frequency resolution, so that the resonance may not be properly resolved. It is possible to overcome this by increasing the distance between sample and antennas. However, to resolve a resonance width of $\delta f = 0.1$ GHz, the time gating should be carried out for a window region (after transforming to the time domain) that is at least $\delta t \sim 1/\delta f = 10$ ns wide. This corresponds to an antenna-to-sample distance of $c\delta t/2 = 1.5$ m. If better resolution is required, this distance could easily increase by a few times, and the setup would quickly become quite large, particularly since a region of the same radius must be cleared of all objects. Alternatively, a large anaechoic chamber may be used, but this is not always available. For a given sample size, the large distance would also increase diffraction around the sample, even if spot-focusing lenses are used.

A calibration procedure that could correct for multiple scattering and diffraction would therefore be needed to overcome the above problems. With such a method, it would also be possible to have a smaller sample size. Not only does this mean a saving in material, but the wavefront would also be more planar over a smaller area, even if lenses are not used. This is an advantage, since the calculation of permittivity and permeability [11] assumes a plane wavefront. A smaller sample leads to larger diffraction which has to be corrected for. The TRL calibration [12], [13] used in [5] cannot be used because it assumes zero diffraction, as in the coaxial case. The "frequency response and isolation" calibration (which we shall call the "simple linear calibration"), which is available in the Hewlett-Packard VNA [13] that we used, could correct for the diffraction, but does not correct for multiple reflection within the cables and connectors.

In this paper, we describe a procedure based on the 16-term error model [14]–[20], which has been used to correct for leakage in microwave measurements of microstrip devices. When applied to free-space measurement, the leakage would correspond to all possible paths of the wave traveling between

Manuscript received June 1, 2005; revised October 12, 2005. This work was supported by the Singapore Defence Science and Technology Agency.

The author is with Temasek Laboratories, National University of Singapore, Singapore 117508 (e-mail: tslhkm@nus.edu.sg).

Digital Object Identifier 10.1109/TMTT.2005.862666

0018-9480/$20.00 © 2006 IEEE

Authorized licensed use limited to: Hlib Zadorozhnyi. Downloaded on November 14,2024 at 17:21:54 UTC from IEEE Xplore. Restrictions apply.

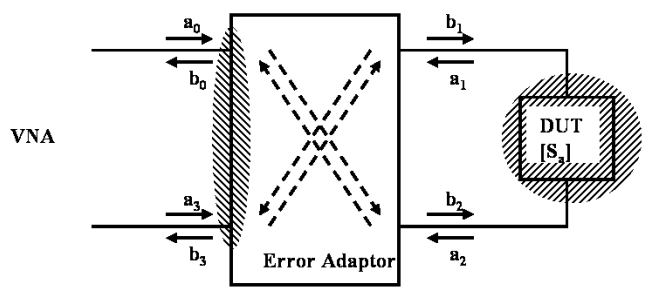

Fig. 1. Schematic diagram of the 16-term error model, showing the possible directions of signal flow between VNA and DUT.

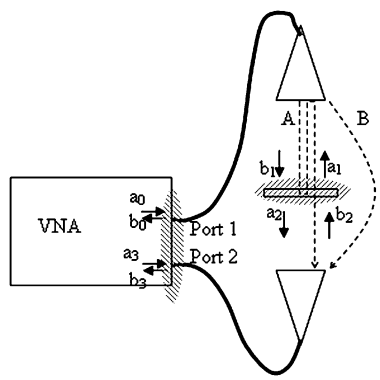

Fig. 2. Schematic diagram for the free-space measurement setup, showing the location of the signals that correspond to the 16-term model in Fig. 1.

the two ports of the VNA that do not go through the sample. These would include diffraction around the edge of the sample and multiple scattering from all surrounding objects. The objective of this paper is a proof of concept that the 16-term model can indeed be applied successfully to free-space measurement.

II. Error Model

The 16-term error model consists of a four-port error box with the vector network analyzer (VNA) on one side and the device under test (DUT) on the other, as shown in Fig. 1. The error box is represented by a 4×4 matrix which relates the values of the signal at each port. This allows for the possibility of direct coupling between the two ports of the VNA, which corresponds to a leakage of microwave energy. On the other hand, the free-space setup consists of a VNA connected to two antennas, with a sample between them, as shown in Fig. 2. The DUT in Fig. 1 corresponds to the sample in Fig. 2. In our case, this is a thin, square sheet of powder composite or metamaterial. The error box corresponds to all of the antennas, cables, and connectors, as well as all space and objects surrounding the sample. The signals entering and leaving each port in Fig. 1 are indicated at their corresponding positions in Fig. 2. Thus, a one-to-one correspondence between the free-space setup and the 16-term error model is possible. The leakage in Fig. 1 between ports 0 and 2 and between ports 1 and 3 corresponds to diffraction around the sample and multiple scattering from surrounding objects (represented by path B) in Fig. 2. The signal flow through sample, antennas, and all connectors corresponds to the flow along the path of ports 0 and 1, the DUT, and ports 2 and 3. Multiple scattering (represented by path A) between them is also taken into account. This is done by relating the signals at each part of the path to the transmission and reflection at each port (or DUT), using the matrix formulation below.

A plausible scheme to apply the 16-term model to free-space measurement is given here.

1) Prepare a few samples with accurately known actual S matrix, S_a. These samples will be called the calibration standards.
2) For each calibration standard, carry out the measurements in the presence of the error box to obtain the measured S matrix, S_m. This refers to the raw data obtained without calibration. In general, it would be different from S_a because of, e.g., multiple scattering at connectors.
3) Use the above data for S_a and S_m to solve for the error box, which can be represented by a 4×4 matrix called the T matrix.
4) Measure the S_m for an unknown sample. Use the T matrix to compute S_a for this sample.

Our implementation of this calibration procedure is discussed in Section III. The mathematics of the 16-term error model is summarized here [17].

1) The signals entering and leaving the four-port error box can be related by the T matrix

$$\begin{bmatrix} b_0 \\ b_3 \\ a_0 \\ a_3 \end{bmatrix} = \mathbf{T} \begin{bmatrix} a_1 \\ a_2 \\ b_1 \\ b_2 \end{bmatrix} = \begin{bmatrix} \mathbf{T}_1 & \mathbf{T}_2 \\ \mathbf{T}_3 & \mathbf{T}_4 \end{bmatrix} \begin{bmatrix} a_1 \\ a_2 \\ b_1 \\ b_2 \end{bmatrix}. \tag{1}$$

2) The notations for the elements in the T matrix are defined here as

$$\mathbf{T} = \begin{bmatrix} t_0 & t_1 & t_4 & t_5 \\ t_2 & t_3 & t_6 & t_7 \\ t_8 & t_9 & t_{12} & t_{13} \\ t_{10} & t_{11} & t_{14} & t_{15} \end{bmatrix}. \tag{2}$$

There are 16 elements which have to be solved for, hence the name 16-term error model.

3) Definition of actual S matrix, S_a, for each sample

$$\begin{bmatrix} a_1 \\ a_2 \end{bmatrix} = \mathbf{S}_a \begin{bmatrix} b_1 \\ b_2 \end{bmatrix} = \begin{bmatrix} S_{a11} & S_{a12} \\ S_{a21} & S_{a22} \end{bmatrix} \begin{bmatrix} b_1 \\ b_2 \end{bmatrix}. \tag{3}$$

4) Definition of measured S matrix, S_m, for each sample

$$\begin{bmatrix} b_0 \\ b_3 \end{bmatrix} = \mathbf{S}_m \begin{bmatrix} a_0 \\ a_3 \end{bmatrix} = \begin{bmatrix} S_{m11} & S_{m12} \\ S_{m21} & S_{m22} \end{bmatrix} \begin{bmatrix} a_0 \\ a_3 \end{bmatrix}. \tag{4}$$

5) Combining the above equations gives

$$\mathbf{T}_1\mathbf{S}_a + \mathbf{T}_2 = \mathbf{S}_m(\mathbf{T}_3\mathbf{S}_a + \mathbf{T}_4). \tag{5}$$

6) This can be rearranged to give (6), shown at the bottom of the following page.
7) Equation (5) can be rearranged to give the actual S parameters

$$\mathbf{S}_a = (\mathbf{T}_1 - \mathbf{S}_m\mathbf{T}_3)^{-1}(\mathbf{S}_m\mathbf{T}_4 - \mathbf{T}_2). \tag{7}$$

Authorized licensed use limited to: Hlib Zadorozhnyi. Downloaded on November 14,2024 at 17:21:54 UTC from IEEE Xplore. Restrictions apply.

The objective of the calibration procedure is to perform enough measurements to solve for all 16 terms in the T matrix. For each calibration standard, four parameters in S_m are measured. This leads to the four equations in (6). Therefore, to solve for the 16 unknowns, there must be at least 16 equations, which require the use of four calibration standards. However, a number of authors have found that the 16 equations from only four calibration standards are not linearly independent [18], [19] because of the nature of the 16-term model, and that unique solution is possible only with at least five standards, which give 20 equations.

In contrast to the 16-term error model, the simple linear calibration, mentioned in Section I, assumes that there is no error box between the VNA and the antennas. However, it does allow for diffraction around the sample. The calibration uses two standards. In the measurement of transmission coefficient, for example, one standard is when there is nothing (THRU) in between the antennas, and the other could be a metal plate (REFL) of the same shape and size as the sample to be measured. With the metal plate, the total signal A_0 due to diffraction and scattering from surrounding objects is measured. This is subtracted from the straight through measurement A_1. Subsequently, when a sample is measured, A_0 is also subtracted from the measured signal A_T. The transmission coefficient is then given by

$$T = (A_T - A_1)/(A_0 - A_1). \tag{8}$$

This calibration ignores multiple reflections within connectors and cables, which could lead to a larger error when diffraction increases. It also cannot correct for the extra multiple scattering, between sample and antennas, that is introduced when there is a sample. This has to be removed by time gating.

Fig. 3 shows the time-domain transmission measurement of a sample of split-ring resonators (SRRs). This is obtained by Fourier transforming the S_{21} data from 2 to 18 GHz. Notice the peak near $t = 2.2$ ns. This can be identified as the first scattering from the antennas (using $ct/2$). This arises because the microwave incident on the sample is partly transmitted and partly reflected. The transmitted part could be scattered from the receiving antenna back to the sample and then reflected back to the receiving antenna. Likewise, the reflected part could be scattered from the transmitting antenna back to the sample and then get transmitted to the receiving antenna, as illustrated by path A in Fig. 2. As the sample is midway between the antennas, both scattering would arrive at the receiving antenna at about the same time. Subsequent features correspond to scattering from surrounding objects. The diffraction component would form a continuous background.

The time gating procedure numerically removes the data beyond a window centered at 0 ns. These may be set to zero or, in the case of the VNA we use, replaced by the time-domain data of a constant unit response from 2 to 18 GHz. We choose the window to be wide enough to retain the time-domain response of the SRR but narrow enough to remove the first reflections from the antennas. However, this could be difficult if the response overlaps with the antenna reflection, as is the case in Fig. 3. When the SRR sample is removed, a narrow peak of 0.1-ns width is observed. When the antenna distance is increased, the peak at 2.2 ns moves to the right. Hence, the broad peak from 0 to 2 ns may be attributed to SRR response.

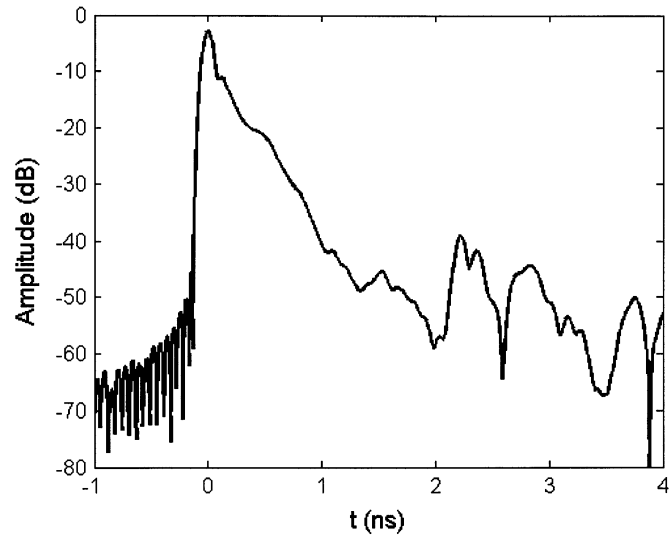

Fig. 3. Transmitted signal in the time domain, after simple linear calibration, through a 15 cm × 15 cm × 5 mm sample of the SRR-c in Fig. 4(b), which is midway between the two antennas separated by 60 cm.

In the calibration procedure described in Section III, all information, which would normally be removed by time gating, would be utilized. The need for time gating is thereby removed, providing a direct solution to the actual S-parameters of the sample—hence, the potential for much improved resolution in the frequency domain.

III. Calibration Procedure

In the application of the 16-term error model to microstrip device measurement, the calibration procedures make use of a large variety of calibration standards. Examples include "through," "short," "line," "match," "load," and "open" [15]–[17]. Some of these are difficult to apply to the free-space setup. For instance, it would be difficult to find a "match" from 2 to 18 GHz in free space, as this would mean a perfect ultrawide-band absorber. The "open" is also difficult. In microstrip measurement, the

$$\begin{bmatrix} S_{a11} & S_{a21} & & & 1 & & & -S_{m11}S_{a11} & -S_{m11}S_{a21} & -S_{m12}S_{a11} & -S_{m12}S_{a21} & -S_{m11} & & -S_{m12} & \\ S_{a12} & S_{a22} & & & & 1 & & -S_{m11}S_{a12} & -S_{m11}S_{a22} & -S_{m12}S_{a12} & -S_{m12}S_{a22} & & -S_{m11} & & -S_{m12} \\ & & S_{a11} & S_{a21} & & & 1 & -S_{m21}S_{a11} & -S_{m21}S_{a21} & -S_{m22}S_{a11} & -S_{m22}S_{a21} & -S_{m21} & & -S_{m22} & \\ & & S_{a12} & S_{a22} & & & & 1 \; -S_{m21}S_{a12} & -S_{m21}S_{a22} & -S_{m22}S_{a12} & -S_{m22}S_{a22} & & -S_{m21} & & -S_{m22} \end{bmatrix} \times \begin{bmatrix} t_0 \\ t_1 \\ \cdots \\ t_{15} \end{bmatrix} = \mathbf{0} \tag{6}$$

Authorized licensed use limited to: Hlib Zadorozhnyi. Downloaded on November 14,2024 at 17:21:54 UTC from IEEE Xplore. Restrictions apply.

open could mean a transmission of 0 and a reflection of $+1$ on the probe. However, in the free-space setup, leaving the antenna aperture open would not give a reflection close to $+1$, because the antenna is designed to match to free space.

On the other hand, the "through" can easily be realized by having no sample between the antennas (THRU). "Short" can be implemented as a reflection, using a thin metal plate (REFL). Their S_a are assumed to be $\begin{pmatrix} 0 & 1 \\ 1 & 0 \end{pmatrix}$ and $\begin{pmatrix} -1 & 0 \\ 0 & -1 \end{pmatrix}$, respectively. For the THRU, this is a definition on which the error correction is based. For the REFL, it is an approximation which should be fairly accurate for a good conductor. The "load" may be implemented using composite materials of metal powder, for example, provided that we know the S_a accurately. With such composites, standard samples of different permittivity and permeability may be fabricated to provide different S_a.

As mentioned in the last section, it is necessary to have at least five calibration standards to solve for the 16 unknowns. We decided to prepare seven standards and use a least square method based on the singular value decomposition (SVD) to solve the equations by minimizing error [21]. Except for the THRU, we need to fabricate six standards. The REFL is fabricated using thin kitchen aluminum (Al) foil to minimize the phase difference on the two sides. The calibration standards were fabricated using different concentrations of copper powder (Cu) or carbonyl iron powder (Fe) in polyurethane (PU). The way that the calibration standards were realized and measured turned out to be crucial. We shall therefore discuss two methods: our initial attempt which failed, and our second attempt which succeeded.

In the first attempt, the PU-Cu and PU-Fe composites were made into square sheets, each with area 15 cm $\times$ 15 cm and thickness 1.75 mm. Each of the samples to be measured after the calibration must have the same area and position, since these would affect the signals in Fig. 2. When each of these sheets was made from a mixture of metal powder and resin, a 7-mm coaxial sample was simultaneously made from the same mixture. The coaxial method was then used to measure the permittivity and permeability of the coaxial sample. With these values, the S_a of the corresponding sheet may then be calculated, by assuming a plane-wave incident normally on an infinitely large sheet with a uniform thickness of 1.75 mm. The S_m of each sheet is also measured. Using the S_m and S_a of all the standard samples, we computed the T matrix. The 16-term model is then applied to measure the S_a of test samples. This is done by first measuring S_m and then calculating S_a with (7). The results are so noisy that nothing meaningful was obtained. We subsequently realize that the results are very sensitive to the accuracy of S_a. A simulation on hypothetical standards shows that an error of 1% in any one of the S_a could produce enough noise to obscure the signal. Errors could have been introduced from many sources in the above process: the powder-resin mixture could be inhomogeneous, the coaxial sample could have gaps in the airline, the 15 cm $\times$ 15 cm sheet may not have uniform thickness, and the radiated field from the antenna is not exactly planar.

In the second attempt, in order to obtain accurate S_a, we decide to measure them *in situ*. This time, each calibration standard is made from two sheets of composites of the same powder and concentration. The dimensions of each sheet remain the same as before. The two sheets are stacked together, with an Al foil of the same area sandwiched in between. This prevents microwave from going through, so S_{a12} and S_{a21} are set to zero. The purpose is to reduce the sources of error. The S_{a11} and S_{a22} are then measured by time gating. This should be reliable because the composites do not have sharp resonances. There is no need to move the load at all between the S_a and the S_m measurements—hence, *in situ*. Thus, there is no need to obtain S_a from a separate measurement of permittivity and permeability, so that all errors associated with these are absent. The *in situ* measurement also means that any imperfection in the load, such as air gaps, nonuniformity in thickness, and even nonplanarity of the wavefront, is irrelevant, as long as the actual and measured S-parameters correspond to the same standard sample. This second attempt turns out to be successful, and we are able to obtain useful results for the SRR measurements, as shown in Section IV. The detailed procedure is given in Appendix C. There, we provide a procedure specific to the HP8722 VNA which we have used, as well as an algebraic procedure suitable for post processing after collection of the raw data.

Once all the S_m and S_a have been measured for the seven standards, the data are recorded on a PC to be used as the basis of error correction for other samples. There are $7 \times 4 = 28$ equations to solve for the 16 unknowns. We use a least square method. First, the equations are arranged in the format minu63pt

$$\mathbf{At} = 0 \tag{9}$$

where $\mathbf{t}$ is a 16×1 column vector containing $t_0, \ldots, t_{15}$, $\mathbf{A}$ is 28×16 matrix containing the coefficients from (6), and 0 is a null vector. The least square result is obtained by solving

$$\mathbf{A}^{+}\mathbf{At} = 0. \tag{10}$$

This is explained in [21] when $\mathbf{A}$ is real and where the equation takes the form

$$\mathbf{A}^{T}\mathbf{At} = 0. \tag{11}$$

In our case, $\mathbf{A}$ is complex, so $\mathbf{A}^T$ generalizes to the Hermitian conjugate $\mathbf{A}^{+}$. Note that

$$\mathbf{A}^{+}\mathbf{At} = 0 \tag{12}$$

is a system of 16 linear equations with 16 unknowns. To obtain a nontrivial solution, we simply remove the last equation, set $t_0 = 1$, and solve for $t_1, \ldots, t_{15}$. This gives the solution $\mathbf{t}$ up to a constant factor. It is not necessary to know this factor as it cancels out in (7) when S_a is calculated from S_m for a test sample measurement.

IV. Results and Discussion

We have tested the error correction method on one carbonyl iron sample and two SRR samples. In order to validate the accuracy, we also made separate measurements on the transmission and reflection coefficient for each of these, using simple linear calibration with time gating. We shall call this the time gating method, and it should be accurate for the carbonyl iron samples which do not have sharp resonance. For the SRR samples, the

Authorized licensed use limited to: Hlib Zadorozhnyi. Downloaded on November 14,2024 at 17:21:54 UTC from IEEE Xplore. Restrictions apply.

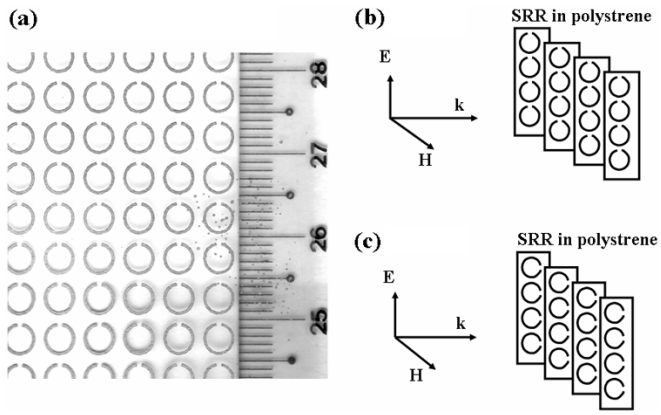

Fig. 4. Fabrication of SRR. (a) Copper clad polyester (LG4014) after etching. The split rings are cut into strips, rotated by 90 deg and stacked together. (b) One way of stacking the split rings. We shall call this configuration SRR-c. (c) Another way of stacking the split rings. We shall call this configuration SRR-u.

accuracy would depend on the width of the resonance. Even if the resolution is poor, the time gating results should be able to reproduce the trends and serve as a guide to check whether that 16-term error correction is correct.

The measurements are made using an HP8722 VNA, at 1601 frequency points at equal intervals from 2 to 18 GHz. The antennas are from Flann Microwave, Woburn, MA—model DP240-AA, bandwidth 2–18 GHz. They are supported vertically, facing each other, on a wooden support. We place the sample horizontally, midway between the two antennas, and on a polystyrene foam board (50 cm $\times$ 50 cm $\times$ 5 cm). The foam board is supported at the edge by wooden strips, and the region between the antennas and foam board is kept clear. The distance of the sample from each antenna is about 30 cm. We use pen marks to indicate the sample position on the foam board. The measurement is carried out in an ordinary room (not an anaechoic chamber).

The dimensions of the PU/Fe sample are 15 cm $\times$ 15 cm $\times$ 1.75 mm. For each SRR sample, the dimensions are 15 cm $\times$ 15 cm $\times$ 5 mm. They are shown schematically in Fig. 4, and are made from laser printing and etching on a flexible circuit material (LG4014 samples from Rogers Corporation). These are then cut into strips and stacked together using polystyrene form spacers. The copper layer on the LG4014 is 20-μm thick, and the polyester film is 50 μm. In the following analysis, we neglect the effect of the polyester film.

As it turns out, the 16-term error correction produces results that generally agree with the time gating results. Fig. 5 shows the results for carbonyl iron. The generally good agreement demonstrates that the 16-term error correction works. Figs. 6 and 7 show the results for the SRR samples. Here, we have also included the results of simulation of a plane-wave incident normally on an infinitely large sample. The simulation method is explained in Appendix A.

The following discrepancies are observed:

1) large oscillations of the 16-term results from 2 to 3 GHz in Figs. 5–7;
2) difference between 16 term results and simulation in Fig. 6(b);

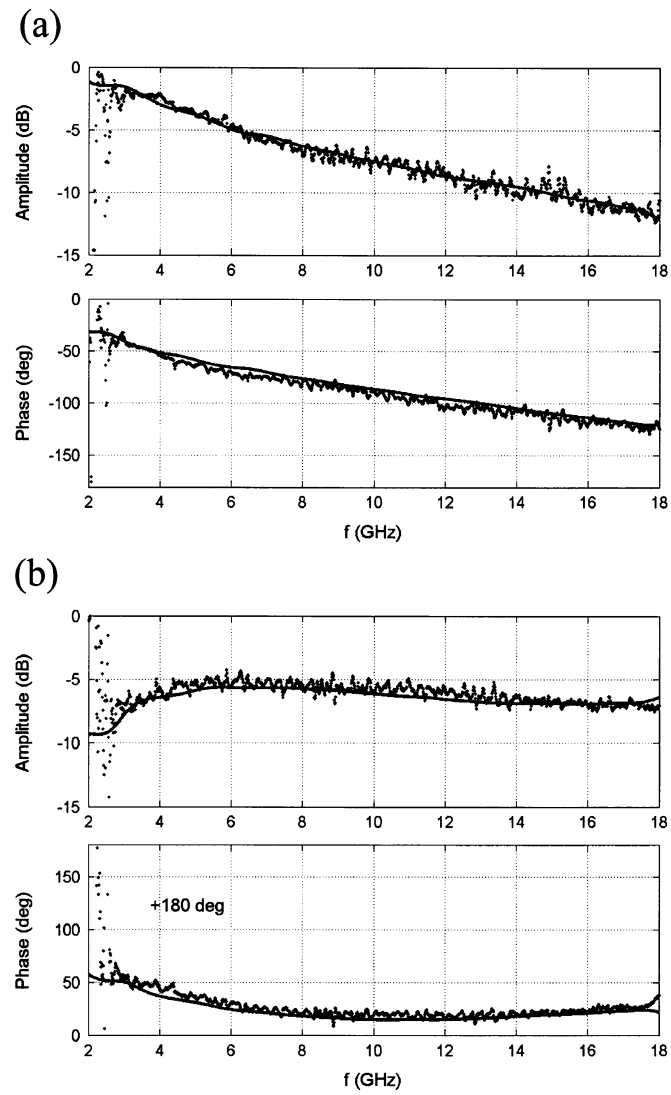

Fig. 5. Measurement results of the PU-Fe sample, with 80.0 wt.% carbonyl iron powder, and dimensions 15 cm $\times$ 15 cm $\times$ 1.75 mm. The solid curve represents the result of the time gating method, and dotted curve that of the 16-term method.

3) noise in Fig. 6(b) which seems significantly larger than those in the other figures;
4) difference between the 16-term results and simulation in Fig. 7(a);
5) large oscillations in the time gating results in Figs. 6(b) and 7(b) from 14 to 18 GHz.

Appendix B suggests some explanations for points 1 to 4, which are summarized here. Point 1 could be due to the S_a of the calibration standards becoming more similar at lower frequency, resulting in greater sensitivity to errors and noise. Points 2 and 3 could both be due to random noise in the VNA and error in sizes and positions of the calibration standards. Point 4 may be explained by the nonplanar nature of the wavefront. Based on this understanding, some improvements could be suggested, which are: 1) fabrication of calibration standards with greater difference in permittivity or permeability; 2) making a sample slot in the foam for accurate positioning, and accurate machining of the calibration standards; and 3) increasing the distance between sample and antennas for flatter wavefronts.

Authorized licensed use limited to: Hlib Zadorozhnyi. Downloaded on November 14,2024 at 17:21:54 UTC from IEEE Xplore. Restrictions apply.

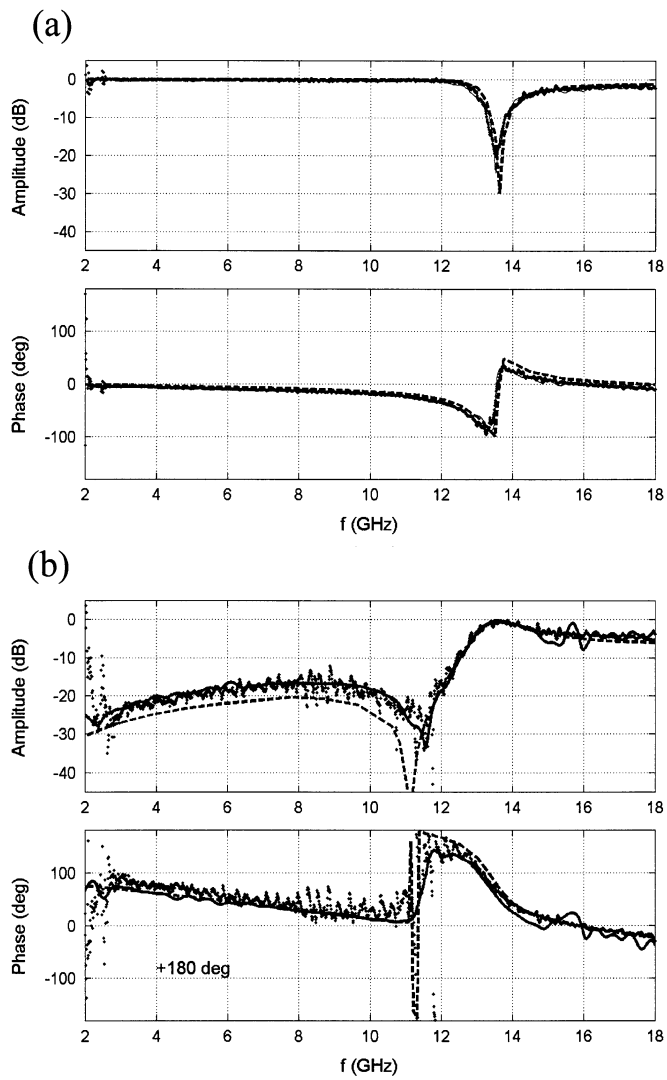

Fig. 6. Measurement results of the SRR-c sample, with dimensions 15 cm × 15 cm × 5 mm. The solid curve represents the result of the time gating method, the dotted curve that of the 16-term method, and the dashed curve shows the simulation result.

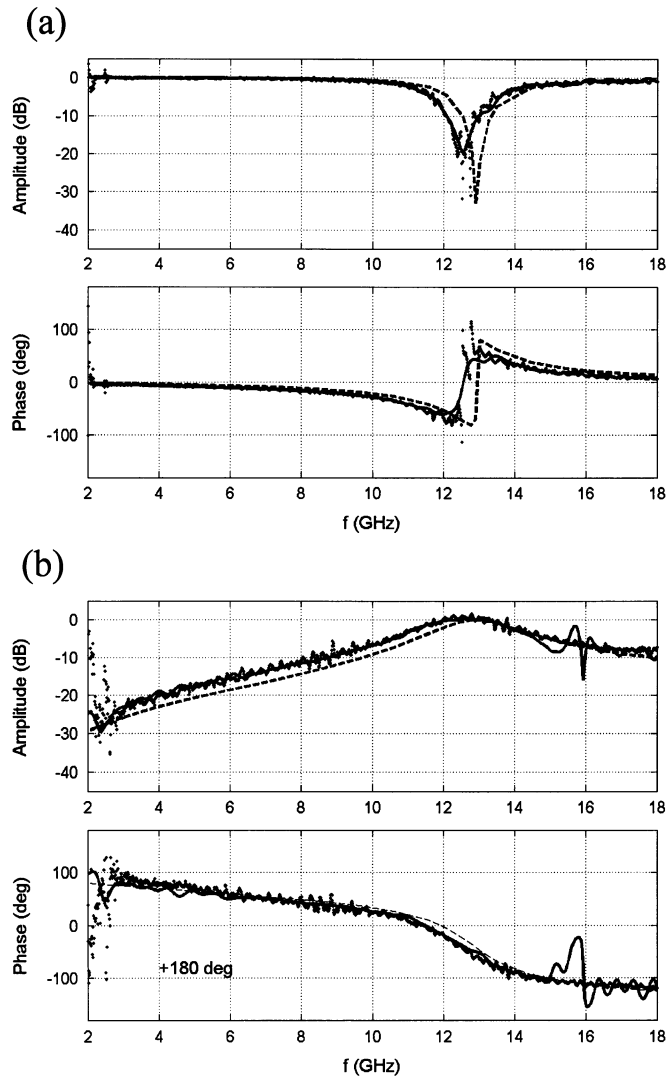

Fig. 7. Measurement results of the SRR-u sample, with dimensions 15 cm × 15 cm × 5 mm. The solid curve represents the result using the time gating method, the dotted curve that of the 16-term method, and the dashed curve shows the simulation result.

To explain point 5), we have carried out a measurement on a separate setup to determine the effect of changing the time gating window. We used two window sizes. The first one is from −2 to 2 ns, which is same as the window size used for the results measurement in Figs. 6 and 7. (This is the minimum size because of the SRR response in Fig. 3. We use from −1 to 1 ns for the S_a of the calibration standards, because their time domain responses are much narrower.) The second window size is from −5 to 5 ns. (For this, the sample–antenna distance must be increased to 1 m.) We found that, when the window size increases, the oscillations from 14 to 18 GHz decreases. This suggests that time gating is the cause of these oscillations. It could be due to multiple scattering from the antennas falling within the window or it could be due to truncating of the SRR response.

We have considered the effect of using fewer calibration standards to simplify the procedure. We found that it is possible to obtain similar agreement by using only five standards, i.e., THRU and REFL plus three others. This is the minimum required to produce a sufficient number of equations. However, not any combination of three out of the five standards gave good results. Some produced more noise than others. The reason for this is not clear at the moment, though it is possible that the permittivity and permeability were too close, so that the resulting equations are not sufficiently independent.

The general agreement in peak width in Figs. 6 and 7 shows that the SRR resonances are sufficiently wide to be properly resolved by the time gating method. While it may appear that the 16 terms are unnecessarily complicated in this case, we must emphasise that this paper is only intended as a proof of concept that the 16-term error correction can be applied to free-space measurement. The full potential of this method may be realized for metamaterials with narrower resonances.

Using an HP8722 VNA, for example, the maximum number of sampling points is 1601 per sweep, from. For 2–18 GHz, this gives only ten points for an interval of 0.1 GHz. Thus, for resonance peak width below 0.1 GHz, not many points on the peak can be recorded if the time gating method is used. It would not be possible to reduce the sweep range to an interval of 0.1 GHz, since a wide bandwidth is required for high-resolution time gating. The 16-term error correction, on the other

Authorized licensed use limited to: Hlib Zadorozhnyi. Downloaded on November 14,2024 at 17:21:54 UTC from IEEE Xplore. Restrictions apply.

hand, performs correction point by point. It does not require a wide bandwidth, except for the measurement of calibration standards S_a. The measured S_a can be interpolated over the small interval around the resonance peak if necessary. This should be reliable since the standards do not have sharp resonances. Thus, the 16-term method offers the possibility to zoom in on narrow peaks for more detailed measurement.

The 16-term method also provides a means to measure the amount of leakage. This can easily be calculated once the T matrix is solved. First,assume a perfectly absorbing sample, so that S_a parameters are all zero. Then suppose that there is only microwave input at a_0 but not a_3. With these conditions, $a_1 = a_2 = a_3 = 0$ in Fig. 1. Since no microwave goes through the sample or gets reflected from it, b_3 must be the leakage. This can be readily solved using (1), and the result is stated here as

$$\frac{b_3}{a_0} = \frac{t_6 t_{15} - t_7 t_{14}}{t_{12} t_{15} - t_{13} t_{14}}. \tag{13}$$

A final point to note is the ease of using the 16-term method. The fabrication of the five standard samples has taken one week, once the metal powders, resin, and molds are ready. The calibration procedure requires the measurement of S_m and S_a for all of the standard samples. Using the HP 8722 VNA with 1601 points per sweep from 2 to 18 GHz, this could be done within an hour. After that, the raw S-parameters of a number of unknown samples may then be measured, each of which would take only a few minutes. The data presented in this paper have been measured on and off over a few hours. The good agreement shows that the calibration does not drift significantly over such a time period. All data are transferred to a computer for processing. Our calibration software is written using MATLAB, and, on a 1-GHz computer, the computation of 1601 points of 16-term results for each sample takes only one to two minutes.

APPENDIX A
SIMULATION

The simulation method used is an extension of the method described in [22]. The reader is requested to refer to [22] for details. We have made the following changes to shorten the simulation time and improve the accuracy.

1) Reference [22] is based on the periodic moment method. It describes a method that can be used to simulate scattering from a two-dimensional (2-D) periodic array of wire elements. Although not stated explicitly, it uses a finite difference approximation of the following relation [23] to compute the E-field due to the current in each segment:

$$\mathbf{E} = -\nabla\phi - \frac{\partial \mathbf{A}}{\partial t}. \tag{A1}$$

The potential ϕ is calculated from the charge distribution on the source segment, which is in turn calculated from the continuity equation [23]

$$\nabla \cdot \mathbf{J} + \frac{\partial \rho}{\partial t} = 0. \tag{A2}$$

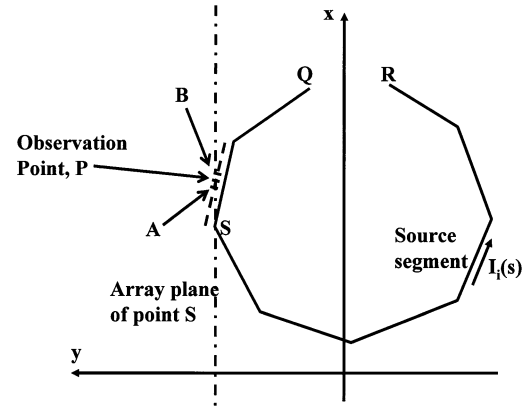

Fig. 8. SRR is approximated as a thin wire consisting of a series of straight segments. Each segment has a current and a charge distribution that produces an E-field on another segment.

Applying this to each segment in the time harmonic case gives

$$\sigma = -\frac{1}{j\omega}\frac{dI}{dx}. \tag{A3}$$

Reference [22] assumes a constant current on each segment. For the isolated segment, this current terminates abruptly at the two ends of the segment, the x derivative in (A3) gives rise to a point charge at each end. This is used to calculate ϕ, while the current I is used to calculate $\mathbf{A}$. [22, eq. (14)] assumes that each point charge is spread out to a line charge of the same length and direction as the segment. In our simulation, we use the point charge instead for better accuracy. However, the use of point charge leads to convergence problems if the observation point (e.g., $\mathbf{P}$ in Fig. 8) falls on or near the array plane of a point charge (e.g., $\mathbf{S}$). While this may be avoided by selecting the observation points carefully, it could be difficult when there are many segments in different directions, as we have found for our SRR elements. This issue is addressed in point 4) below.

2) In [22], the potential gradient in (A1) is approximated by computing the potential at each end of an observation segment, and then dividing the difference by the length of the segment. Since we are using the point matching method, we compute the potential at a much smaller distance from the observation point instead for greater accuracy. We select the observation point, P, to be near the centre of the observation segment. We then choose two points ($\mathbf{A}$ and $\mathbf{B}$ in Fig. 8) that are separated by 1/10 of the segment length and such that the line joining them is parallel to the segment and contains $\mathbf{P}$. The potentials are then computed at these two points, and the difference divided by the distance between them.

3) In order to reduce the number of segments required, we make use of the basis functions in [24]. We shall call these the NEC basis functions. They represent the current in each segment by means of the following linear combination:

$$I_i = A_i + B_i \sin k(s - s_i) + C_i \cos k(s - s_i). \tag{A4}$$

Authorized licensed use limited to: Hlib Zadorozhnyi. Downloaded on November 14,2024 at 17:21:54 UTC from IEEE Xplore. Restrictions apply.

The charge distribution is derived from this using (A3). Note that the sudden change to zero at each end of an isolated source segment also gives rise to a point charge there. In addition, the sine and cosine components give rise to corresponding line charge distributions of the segment. These are not present in the original [22] formulation, but can be computed readily from (A3). The plane-wave sums for the sine and cosine current and line charge components can be derived in a similar way to those for the constant current and line charge, as in [22].

4) Using the NEC basis functions, the condition that the current between adjacent segments is continuous is enforced. This also means that the effect of the point charges at the common end of adjacent segments cancels. This is because the equality of the current on two sides of the common end gives rise to equal and opposite point charges on the two sides, according to (A3). Thus, all point charges, except for the two at the extreme ends ($\mathbf{Q}$ and $\mathbf{R}$ in Fig. 8) of the whole wire element, can be ignored. This greatly alleviates the problem, mentioned in point 1) above of selecting observation points to avoid array planes containing the point charges.
5) For each segment, we take into account the skin effect by assuming an impedance per unit length equal to that of an infinitely long cylinder [25] of the same radius as the equivalent radius of the wire and the same resistivity as copper.

We have developed a code based on the above modifications. To carry out the simulation, the copper strip of each SRR element must be approximated with a thin wire. First, the following parameters for an SRR element are obtained by magnifying and measuring the image in Fig. 4(a):

- width of copper strip $= 0.2578$ mm;
- outer radius of SRR $= 3.7031$ mm;
- inner radius of SRR $= 3.4549$ mm;
- angle subtended by gap at center $= 9.610°$.

Assuming that the array plane is in the xz-plane and that the plane of each element is in the xy-plane (as in Fig. 8), the inter-element spacings are measured to be 4.8 mm in the x-direction and 5.0 mm in the z-direction. In our simulation, a thin wire approximation is used. The following parameters are used for the thin wire element:

- number of segments $= 8$;
- equivalent thin wire radius = width of copper strip/4;
- radius of thin wire SRR $= 3.7031$ mm;
- angle subtended by gap at center $= 9.610°$ (no change).

The printed copper strip has a thickness of 20 μm (as given in the specification of the LG4014), which is small compared with the strip width of the difference between the outer and inner SRR radii above. We thus take the equivalent thin wire radius to be one quarter of the width of the copper strip [26]. It would seem more reasonable to take the radius of the thin wire SRR to be the average of the inner and outer radii of the original copper strip SRR. However, the resulting simulation gives resonance peaks that are about 0.5 GHz higher. The use of the outer radius gives much better agreement, as shown in Figs. 6 and 7. The reason could be due to the inaccuracy arising from approximating of the flat strip to a thin wire. This is the only "fitting" that was done in the whole simulation.

The remaining factors considered in the simulation are as follows. A copper resistivity of 1.68×10^{-8} Ω·m is used. Without this and the impedance introduced in point 5) above, the resonance peaks would be much sharper. The polystyrene foam used to make the spacers for the SRR is measured to have a permittivity of 1.075. After simulation, the frequency is divided by the square root of this value to correct for wavelength changes inside the foam. This causes a shift of about 0.5 GHz of the resonance peaks to the lower frequency. This treatment neglects multiple reflections at the foam–air interface, which is hopefully small. Next, the end cap current in the thin wire approximation is assumed to be zero. Reference [24] provides a formula for approximating the current flowing into the circular area at each end of a cylindrical thin wire, i.e., the end cap. Since we are actually simulating for a flat copper strip, whose end cap area is much smaller than that of a cylindrical wire with the equivalent radius given above, we have set the current at each end of the thin wire to zero. Finally, for comparison with experiment, the xz-plane in the simulation has to be shifted to the same position as the reference plane used in the measurement, i.e., the side of the REFL standard (Al foil) facing the incident beam. This corresponds to an offset of 2.5 mm from the center of the SRR elements in the case of the SRR-c sample and an offset of 3.5 mm in the case of the SRR-u (because of the way they are fabricated).

Using the above method and parameters, we have carried out the simulation and obtained the results in Figs. 6 and 7, which agree quite well with the measurement. The main discrepancies are in Figs. 6(b) and 7(a), and some explanations for these are offered in Appendix B. (Note that we have assumed that the effect of the polyester film is small and have neglected it in the simulation.)

Appendix B
Error Analysis

In Appendix-B.A, we analyze the error due to the measurement process. The objective of this paper is to measure the material property, which can often be related to the transmitted and reflected coefficients of incident plane wave. In Figs. 6 and 7, for instance, reasonable agreement with the simulation of plane-wave incidence is obtained. Thus, in Appendix-B.B, we also discuss the effect of deviation from a planar wavefront.

A. Measurement Error

The possible sources of measurement errors are random noise and constant bias in the S-parameters due to the VNA, and errors in sizes and positions of the calibration standards and samples. We check that the effect of constant bias is small by measuring a test sample of Teflon using the time gating method. The resulting permittivity of 2.05±0.05 from 2 to 18 GHz agrees closely with published result [26]. We next compare error due to the calibration standards and to random noise as follows.

First, we take the difference between the S_{21} of each calibration standard, and the S_{21} of the REFL standard. We find that an estimate of this error using the expressions in point 4) below provides a reasonable bound for this measured S_{21} difference. We then postulate that the errors depend more on the areas of

Authorized licensed use limited to: Hlib Zadorozhnyi. Downloaded on November 14,2024 at 17:21:54 UTC from IEEE Xplore. Restrictions apply.

the standards and less on their positions, provided that the errors in both are small compared to their dimensions. We test this hypothesis by estimating the error bounds due to the areas as follows.

1) First, let the T matrix computed and used in Figs. 5–7 be the actual T matrix.
2) Assume that the S_a of the calibration standards measured by the time gating method are the true S_a.
3) Compute the "accurate" S_m of the calibration standards from these, using (5).
4) Introduce error into the area of each standard sample. As the standards are fabricated using a ruler, there is an error of ± 1 mm on each side of the 150 mm $\times$ 150 mm area. This gives a fractional error in the area of $da = \pm 0.0134$, which in turn gives rise to errors in S_m and S_a. Taking the REFL as the reference, the error would refer to the difference of the standard sample and the area of the REFL standard. We define the following symbols:

$$A_0 = S_{m11} \text{ of THRU}$$
$$A_1 = S_{m11} \text{ of Al foil (REFL)}$$
$$B_1 = S_{m21} \text{ of THRU}$$
$$B_0 = S_{m21} \text{ of Al foil (REFL)}$$
$$A_R = S_{m11} \text{ of a calibration standard.}$$

The simple linear calibration of S_a is then given by $S_{a11} = (A_R - A_0)/(A_1 - A_0)$, since A_0 is the reflection background when there is no sample. This is before time gating. Since we only require an error estimate, this value should be sufficient as an estimate of S_a. Note that S_m of THRU and REFL are the reference standards, thus, they have no area errors. The errors in each calibration standard are then approximated by

$$S_{m11}\text{error} \approx da \times S_{m11}$$
$$S_{m21}\text{error} \approx -da \times (B_1 - B_0)$$
$$S_{a11}\text{error} \approx da \times S_{a11}.$$

The first expression is true because S_{m11} is the reflection, so if the area increases by a fraction of da, so would S_{m11}. The second expression is true because $(B_1 - B_0)$ is the microwave going through the sample area when there is no sample, whereas S_{m21} is the microwave going around this area. (Recall that the calibration standard has a sandwiched Al foil, so microwave cannot go through it.) If the standard area is reduced by da, assuming that the microwave is roughly uniform over the area, then the amount going around the area will be increased by da of that amount. The third expression is true because, as given above, S_{a11} is related to A_R, which is S_{m11} of the standard, so it would have at least a similar error to S_{m11}. We assume that there is no error in S_{a21} since it is zero because of the sandwiched Al foil. These errors are added to S_m and S_a to create the perturbed S-parameters.
5) The perturbed S_m and S_a are used to compute the perturbed T matrix using the method described in the last paragraph of Section III.

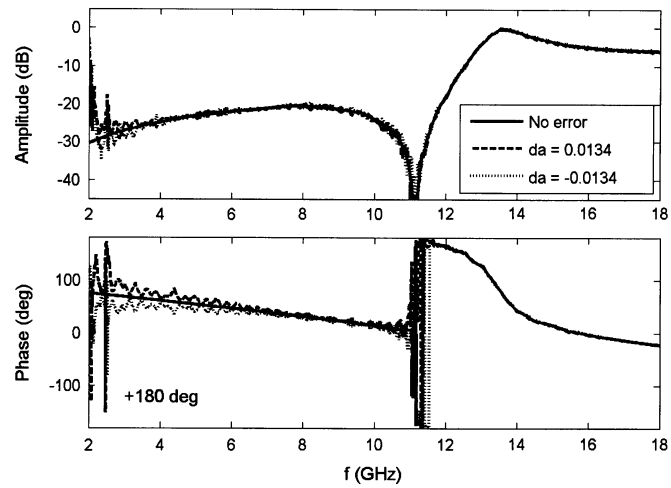

Fig. 9. Error bounds for the 16-term measurement of the reflection from the SRR-c sample, due to errors in the areas of the calibration standards.

6) The ideal S_m of the SRR samples are computed from the unperturbed T matrix from point 1) above, and the simulated S_a in Figs. 6 and 7 with the help of (5).
7) The perturbed S_a is then compute from this ideal S_m, and the perturbed T matrix from point 5), using (7).

The result of this simulation for the reflection of the SRR-c sample is shown in Fig. 9. Notice that the error bounds agree fairly well with the noise magnitudes in Fig. 6(b) below 6 GHz. This partially justifies the above hypothesis that standards sizes are the main sources of error. We shall not analyze the error due to position here as this depends on the antenna radiation pattern and multiple scattering, which is quite complex. Instead, we shall show later that the error above 6 GHz may be attributable to random noise in S_m.

Even the large oscillation near 2 GHz of Fig. 6(b) is reproduced clearly in Fig. 9. This provides one explanation for this oscillation—if the standards size errors can be reduced, this oscillation may also decrease. However, it cannot explain why the oscillation does not occur at other frequencies. One possible reason is that the S_a, and hence the S_m, of the calibration standards, approach one another quite closely at lower frequencies. As a result, the (6) from one standard becomes more similar to those of another standard, so that the solution becomes more sensitive to errors (e.g., if two intersecting straight lines on a graph are nearly parallel, a small shift in one line would cause a large shift in the point of intersection.)

Next, we consider the noise in the S-parameters. By observing the time gated S_{a21} in the THRU configuration over a period of a few hours, we notice that a drift of up to 0.25 dB is possible. In fact, for a VNA, the uncertainty could depend on frequency, the S-parameter, its value, and the connector type. As we only wish to know whether the S-parameter noise is a significant source of error, we ignore this complex dependence and simply add a random noise with magnitude between $dS = \pm 0.2$ dB to all of the S_a and S_m. We repeat the calculation from points 1) to 7) above, except that point 4) is replaced by adding a random noise to the magnitude of each S-parameter. (We did not perturb the phase.) Fig. 10 shows the result. The noise level above 6 GHz agrees fairly well with

Authorized licensed use limited to: Hlib Zadorozhnyi. Downloaded on November 14,2024 at 17:21:54 UTC from IEEE Xplore. Restrictions apply.

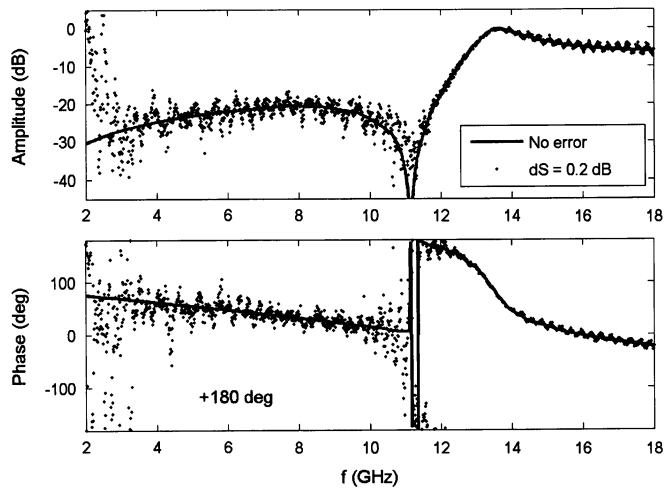

Fig. 10. Error bounds for the 16-term measurement of the reflection from the SRR-c sample, due to errors in the random noise of the measured S-parameters.

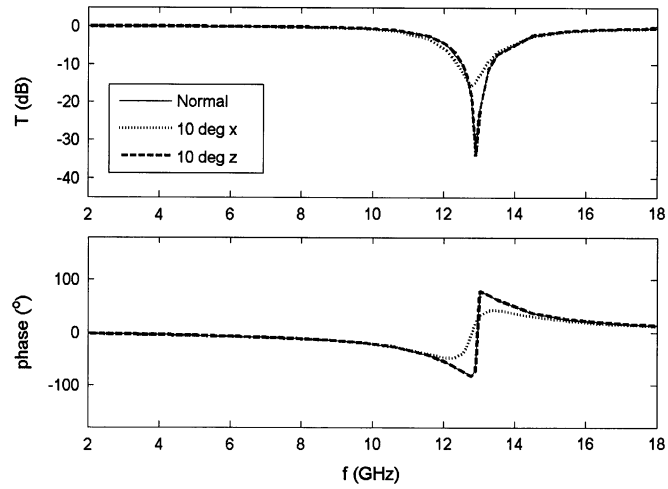

Fig. 11. "Error bounds" for the transmission through the SRR-u sample, due to error in incident direction of a plane wave of 10° from normal.

the noise magnitudes in Fig. 6(b). The errors below 6 GHz are larger than the observed noise in Fig. 6(b), suggesting that the noise level there is below 0.2 dB.

B. Wavefront Error

The actual shape of the wavefront incident on the sample is not likely to be planar because of the proximity to the antennas and is likely to depend in a complex way on the antenna properties and the multiple scattering. Reference [28] provides a detailed analysis on the effect of a Gaussian beam on the measured transmission and reflection. Here, we use a simpler way to give an estimate on the effect of deviation from a planar wavefront. We consider that the actual wavefront as approximately the sum of a number of planar wavefronts incident in different directions.

We next suppose that the maximum deviation may be estimated by considering the angle subtended by the sample at the antenna feed point. As this is about 20° for our experimental setup, the maximum incidence angle, with respect to normal, is taken as 10°. We then simulate of the transmission and reflection of incident plane waves at this angle for two cases: when the plane of incidence is in the xy-plane and when it is in the yz-plane. The transmission result for the SRR-u sample is shown in Fig. 11. Notice that the result for 10° incidence angle in the xy-plane actually offers a better agreement with the 16-term measurement result in Fig. 7(a). This partly justifies the estimate of 10° wave-front deviation above and provides a possible explanation for the discrepancy between simulation and experiment in Fig. 7(a).

We now comment on the cases not discussed above—the measurement error for SRR-c transmission, SRR-u transmission and reflection, and the wavefront error for SRR-u reflection, SRR-c transmission and reflection. In all of these, the error bounds simulated using the above methods are much closer to the "accurate" result than those shown in Figs. 9–11. This is consistent with the fact that the corresponding cases in Figs. 6 and 7 also show better agreement between measurement and simulation. In particular, note that error in the time gating results from 14 to 18 GHz in Figs. 6(b) and 7(b) greatly exceeds those of the 16-term results, demonstrating the reliability of the 16-term method.

Appendix C
16-Term Procedure

A. Using HP8722 VNA

The specific procedure we have followed using the HP8722 VNA is presented here. The terminologies (in italics) used are therefore instrument specific and are explained in [13]. We list the steps required to obtain the all the S_a and S_m of the calibration standards required for computing the T matrix.

Step 1) Do *response-isolation* calibration with *time gating* (*time span* 2 ns in our case) for S_{11} reflection and *save state*. Use Al foil for *response*, and nothing for *isolation*.

Step 2) *Do response-isolation* calibration with *time gating* for S_{22} reflection and *save state*. Use Al foil for *response*, and nothing for *isolation*.

Step 3) Switch off *error correction*. Measure S_m of THRU and REFL.

Step 4) Switch on *error correction*. For each of the remaining calibration standard first measure S_m.

Step 5) Without moving the load, recall the *state* in Step 2) and measure S_{11}.

Step 6) Then recall the *state* in Step 3) and measure S_{22}.

Step 7) Since $S_{12} = S_{21} = 0$, Steps 5) and 6) give the S_a of the calibration standard.

B. Raw Data Processing

Alternatively, it is possible to collect the S_m for all of the calibrations standards first, and then process these on a PC. We do not know how exactly the HP VNA implements its response-isolation calibration and time gating. However, we have checked that the result of the simple linear calibration and time gating procedures suggested below matches closely with corresponding results of the HP VNA. We thus propose the following 16-term calibration procedure, which should lead to results similar to ours.

Step 1) Let S_m^i be the measured S_m parameters of the ith calibration standard, measured by a VNA without any calibration. Thus $i = 1, \ldots, 7$ in our case, where $i = 1$ is for THRU, and $i = 2$ is for REFL.

Authorized licensed use limited to: Hlib Zadorozhnyi. Downloaded on November 14,2024 at 17:21:54 UTC from IEEE Xplore. Restrictions apply.

Step 2) S_m^i is measured at N points at regular intervals from $f_{\min}$ to $f_{\max}$. In our case, $f_{\min} = 2$ GHz, $f_{\max} = 18$ GHz, and $N = 1601$. The frequency interval is $\delta f = (f_{\max} - f_{\min})/(N-1)$.

Step 3) Thus, for each S_m^i, there are four series of data: $S_{m11}^i[n], S_{m21}^i[n], S_{m12}^i[n]$ and $S_{m22}^i[n]$ for $n = 1, \ldots, N$. Each n is associated with the frequency $f[n] = (n-1)\delta f + f_{\min}$.

Step 4) To perform the simple linear calibration, let $A_0 = S_{m11}^1$, and $A_1 = S_{m11}^2$. Let $A_R^i = S_{m11}^i$. Compute $R^i = (A_R^i - A_0)/(A_1 - A_0)$. Note that $R^1 = 0$ and $R^2 = 1$.

Step 5) To perform time gating, some preparatory work is required. First define a discrete signal $H[n]$. Let $H[n]$ be $R^2[n]$, which is 1, for $n = 1, \ldots, N$.

Step 6) Extend this signal to $N_1 = 10(N-1)$ by zero padding. Thus $H[n] = 1$ for $n = 1, \ldots, N$, and $H[n] = 0$ for $n = N+1, \ldots, N_1$.

Step 7) Perform a discrete Fourier transform (DFT) [21] to give

$$h[m] = \sum_{n=1}^{N_1} H[n] \exp(2\pi j m n / N_1) \tag{C1}$$

for $m = -N_1/2, \ldots, N_1/2 - 1$.

Step 8) $H[m]$ is approximately a sinc function. Define the corresponding time $t[m] = m\delta t$, where $\delta t = 1/(N_1 \delta f)$.

Step 9) To perform time gating on R^i $(i = 3, \ldots, 7)$, repeat Steps 5)–7), with $H[n]$ replaced by $R^i[n]$. Let the resulting DFT be $r^i[m]$. It is here that the multiple scattering peaks from antennas are resolved.

Step 10) Specify a time t_0 (1 ns in our case) that is smaller than the time for the first reflection from the antenna. It is best to plot $r^i[m]$ against $t[m]$ graphically to see the peaks and decide.

Step 11) Let m_0 be the largest integer for which $t[m_0] < t_0$. Define a new signal $s^i[m]$. $s^i[m]$ is obtained by replacing $h[m]$ by $r^i[m]$ for $|m| \leqslant m_0$.

Step 12) Perform the inverse DFT to give

$$S^i[n] = \frac{1}{N_1} \sum_{m=-N_1/2}^{N_1/2-1} s^i[m] \exp(-2\pi j m n / N_1) \tag{C2}$$

for $n = 1, \ldots, N$.

Step 13) This gives $S_{a11}^i[n] = S^i[n]$ for $n = 1, \ldots, N$.

Step 14) Now repeat Steps 4)–13), replacing A_R^i by S_{m22}^i, A_0 by S_{m22}^1 and A_1 by S_{m22}^2. This gives $S_{a22}^i[n] = S^i[n]$.

Step 15) Together with $S_{a21}^i[n] = S_{a12}^i[n] = 0$, these give S_a^i.

Step 16) Steps 4)–15) are repeated for $i = 3$ to 7 to obtain all the S_a. (Remember that S_a^1 and S_a^2 are defined as in Section III for THRU and REFL.)

ACKNOWLEDGMENT

The author would like to thank Dr. C. Linfeng, University of Arkansas, Fayetteville, for teaching the coaxial measurement method and Dr. S. M. Matitsine, Temasek Laboratories, National University of Singapore, Singapore, for helpful discussion. The author would also like to thank DSO National Laboratories, Singapore, and the Center for Superconducting and Magnetic Materials, National University of Singapore, for providing the microwave measurement facilities, and DSO for providing the carbonyl iron powder, Makin Metal Powders, Rochdale, U.K., for providing the copper powder, and Rogers Corporation, Singapore, for providing the copper clad polyester.

REFERENCES

[1] D. R. Smith, D. C. Vier, N. Kroll, and S. Schultz, "Direct calculation of permeability and permittivity for a left-handed metamaterial," *Appl. Phys. Lett.*, vol. 77, no. 14, pp. 2246–2248, Oct. 2000.

[2] T. Weiland, R. Schuhmann, R. B. Greegor, C. G. Parazzoli, A. M. Vetter, D. R. Smith, D. C. Vier, and S. Schultz, "*Ab initio* numerical simulation of left-handed metamaterials: Comparison of calculations and experiments," *J. Appl. Phys.*, vol. 90, no. 10, pp. 5419–5424, Nov. 2001.

[3] P. Gay-Balmaz and O. J. F. Martin, "Electromagnetic resonances in individual and coupled split-ring resonators," *J. Appl. Phys.*, vol. 92, no. 5, pp. 2929–2936, Sep. 2002.

[4] C. R. Brewitt-Taylor, P. G. Lederer, F. C. Smith, and S. Haq, "Measurement and prediction of helix-loaded chiral composites," *IEEE Trans. Antennas Propag.*, vol. 47, no. 4, pp. 692–700, Apr. 1999.

[5] D. K. Ghodgaonkar, V. V. Varadan, and V. K. Varadan, "Free-space measurement of complex permittivity and complex permeability of magnetic materials at microwave frequencies," *IEEE Trans. Instrum. Meas.*, vol. 39, no. 2, pp. 387–394, Apr. 1990.

[6] A. Amiet and P. Jewsbury, "Free space microwave permittivity and permeability measurements," in *Proc. Microw. Conf.*, Dec. 3–6, 2000, pp. 445–448.

[7] J. Musil and F. Zacek, *Microwave Measurements of Complex Permittivity by Free-Space Methods and Their Applications*. New York: Elsevier, 1986, pp. 44–60, 92–166.

[8] A. L. Cullen, "A new free-wave method for ferrite measurement of millimeter wavelengths," *Radio Sci.*, vol. 22, no. 7, pp. 1168–1170, Dec. 1987.

[9] E. J. Vanzura, J. R. Baker-Jarvis, J. H. Grosvenor, and M. D. Janezic, "Intercomparison of permittivity measurements using the transmission/reflection method in 7 mm coaxial transmission lines," *IEEE Trans. Microw. Theory Tech.*, vol. 42, no. 11, pp. 2063–2070, Nov. 1994.

[10] L. F. Chen, C. K. Ong, C. P. Neo, V. V. Varadan, and V. K. Varadan, *Microwave Electronics: Measurement and Materials Characterization*. Chichester, U.K.: Wiley, 2004, pp. 182–187.

[11] W. B. Weir, "Automatic measurement of complex dielectric constant and permeability at microwave frequencies," *Proc. IEEE*, vol. 62, no. 1, pp. 33–36, Jan. 1974.

[12] R. A. Soares, P. Gouzien, P. Legaud, and G. Follot, "A unified mathematical approach to two-port calibration techniques and some applications," *IEEE Trans. Microw. Theory Tech.*, vol. 37, no. 11, pp. 1669–1674, Nov. 1989.

[13] *User's Guide—Agilent Technologies—8719ET/20ET/22ET-8719ES/20ES/22ES-Network Analyzers*, Agilent Technol., Palo Alto, CA, Jun. 2002. Part 08 720-90392. [Online]. Available: http://www.agilent.com, pp. 6–10, 6–11, 6–17–6–21.

[14] D. K. Rytting, "Improved RF hardware and calibration methods for network analyzers," *Proc. RF Microw. Meas. Symp. Exhib.*, pp. 1–14, 1991.

[15] H. Heuermann and B. Schiek, "15-term self-calibration methods for the error-correction of on-wafer measurements," *IEEE Trans. Instrum. Meas.*, vol. 46, no. 5, pp. 1105–1110, Oct. 1997.

[16] ——, "Results of network analyzer measurements with leakage errors-corrected with direct calibration techniques," *IEEE Trans. Instrum. Meas.*, vol. 46, no. 5, pp. 1120–1127, Oct. 1997.

[17] K. Silvonen, "LMR 16-a self-calibration procedure for a leaky network analyzer," *IEEE Trans. Microw. Theory Tech.*, vol. 45, no. 7, pp. 1041–1049, Jul. 1997.

[18] K. J. Silvonen, "Calibration of 16-term error model [microwave measurement]," *Electron. Lett.*, vol. 29, no. 17, pp. 1544–1545, Aug. 1993.

Authorized licensed use limited to: Hlib Zadorozhnyi. Downloaded on November 14,2024 at 17:21:54 UTC from IEEE Xplore. Restrictions apply.

[19] J. V. Butler, D. K. Rytting, M. F. Iskander, R. D. Pollard, and M. V. Bossche, "16-term error model and calibration procedure for on-wafer network analysis measurements," *IEEE Trans. Microw. Theory Tech.*, vol. 39, no. 12, pp. 2211–2217, Dec. 1991.

[20] H. Van Hamme and M. V. Bossche, "Flexible vector network analyzer calibration with accuracy bounds using an 8-term or a 16-term error correction model," *IEEE Trans. Microw. Theory Tech.*, vol. 42, no. 6, pp. 976–987, Jun. 1994.

[21] W. H. Press, S. A. Teukolsky, W. T. Vetterling, and B. P. Flannery, *Numerical Recipes in C, The Art of Scientific Computing*, 2nd ed. Cambridge, U.K.: Cambridge Univ. Press, 2002, pp. 503, 671–681.

[22] H. K. Schuman, D. R. Pflug, and L. D. Thompson, "Infinite planar arrays of arbitrarily bent thin wire radiators," *IEEE Trans. Antennas Proag.*, vol. 32, no. 4, pp. 364–377, Apr. 1984.

[23] J. D. Jackson, *Classical Electrodynamics*. New York: Wiley, 1999, p. 3, 239.

[24] J. Burke and A. Poggio. (1981. UCID 18 834. [Online]. Available: http://www.nec2.org, Jan.) *Numerical Electromagnetics Code (NEC)—Method of Moments, Part I: Program Description—Theory*

[25] S. Ramo, J. R. Whinnery, and T. Van Duzer, *Fields and Waves in Communication Electronics*, 3rd ed. New York: Wiley, 1994, pp. 180–185.

[26] O. Einarsson, "The wire," in *Electromagnetic and Acoustic Scattering by Simple Shapes*, J. J. Bowman, T. B. A. Senior, and P. L. E. Uslenghi, Eds. New York: Hemisphere, 1987, pp. 472–502.

[27] J. Baker-Jarvis, E. J. Vanzura, and W. A. Kissick, "Improved technique for determining complex permittivity with the transmission/reflection method," *IEEE Trans. Microw. Theory Tech.*, vol. 38, no. 8, pp. 1096–1103, Aug. 1990.

[28] L. E. R. Petersson and G. S. Smith, "An estimate of the error caused by the plane-wave approximation in free-space dielectric measurement systems," *IEEE Trans. Antennas Propag.*, vol. 50, no. 6, pp. 878–887, Jun. 2002.

Kai Meng Hock was born in Singapore, in 1966. He received the B.A. (Hons.) and Ph.D. degrees from Cambridge University, Cambridge, U.K., in 1988 and 1992, respectively, both in physics.

From 1992 to 1997, he was with DSO National Laboratories, Singapore, where he was involved with optical engineering and signal processing. From 1997 to 2001, he was a Principal Engineer with the Sony Singapore Research Laboratory, where he was involved with servo control and read/write mechanism of optical disc systems He is currently a Principal Research Scientist with Temasek Laboratories, National University of Singapore, Singapore. His research interest is in microwave materials.

Authorized licensed use limited to: Hlib Zadorozhnyi. Downloaded on November 14,2024 at 17:21:54 UTC from IEEE Xplore. Restrictions apply.